

High-temperature oxide ceramic microwave absorber enabled by thermionic migration mediated by electron delocalization

Received: 1 October 2024

Accepted: 9 September 2025

Published online: 16 October 2025

Check for updates

Ruopeng Cui^{1,4}, Zewen Duan^{1,4}, Yi Li², Xuefei Zhang¹, Xiangyang Liu¹, Guang Yang¹, Lihong Yang¹, Biao Zhao³✉ & Chunlei Wan¹✉

The escalating demand for long-term high-temperature microwave-absorbing materials (HTMAMs) in high-speed aerospace stealth is hindered by limitations such as magnetic loss degradation or oxidation risks. Herein, we introduce rare earth zirconate ceramics that exhibit air stability up to 1600 °C. Abundant oxygen vacancies significantly enhance permittivity and thus microwave-absorbing performance through activated thermionic migration at elevated temperatures. Moreover, the thermionic-facilitated permittivity can be meticulously modulated by electron delocalization, with the extent governed by lattice disorder. We demonstrate this concept through a dual-layer Er₂Zr₂O₇/Gd₂Zr₂O₇ structure to further optimize impedance matching, achieving an ultra-wide bandwidth (8.27 GHz) and strong absorption (−64.61 dB) at ultra-thin thicknesses under 1.2 mm at 600 °C mainly by macroscopic interfacial resonance, alongside an ultralow thermal conductivity (1.61 W·m^{−1}·K^{−1}). This work presents an innovative approach to design high-performance and anti-oxidative HTMAMs through thermionic migration tuned by electron delocalization, advancing structural-functional integrated materials for extreme environments.

Nowadays, microwave-absorbing materials, which can effectively attenuate microwaves at gigahertz (GHz) frequencies, have appealed increasing attention worldwide due to their indispensable role in various cutting-edge fields, including electromagnetic pollutant elimination, microwave communication, information security, and most importantly, electromagnetic stealth for sensitive equipment such as aerospace vehicles^{1–5}. Particularly, as the velocity of aerospace vehicles has become significantly faster, more equipment on high-speed aerospace vehicles, e.g. aerospace engines and gas turbines, are confronted with the strongly oxidant environment at much elevated temperatures for a long time aside from the radar detection^{6–8}. Hence, there is an urgent need for the desirable high-temperature microwave-absorbing materials (HTMAMs) that can withstand the long-term adverse atmosphere.

As is well known, microwave-absorbing materials (MAMs) can be categorized into two types: magnetic-loss-dominated or dielectric-loss-dominated MAMs^{4,9}. Although magnetic-loss-dominated MAMs, mainly ferromagnetic materials, generally obtain more outstanding room-temperature microwave-absorbing performance, these materials are not suitable for devising HTMAMs owing to their weakening magnetic loss properties with increasing temperatures (especially above the Curie points)^{10–12}. As for dielectric-dominated MAMs, carbon-based materials have been mostly studied for room-temperature microwave absorption due to their diversified and tunable dielectric loss mechanisms⁴. However, these materials are very susceptible to oxidation above 400 °C, hampering their applications in high-temperature microwave absorption^{2,13,14}.

¹State Key Laboratory of New Ceramics and Fine Processing, School of Materials Science and Engineering, Tsinghua University, Beijing, China. ²College of Mathematics and Physics, Beijing University of Chemical Technology, Beijing, China. ³School of Microelectronics, Fudan University, Shanghai, China. ⁴These authors contributed equally: Ruopeng Cui, Zewen Duan. ✉e-mail: zhao_biao@fudan.edu.cn; wanccl@mail.tsinghua.edu.cn

In contrast, ceramic-based materials, which can generally maintain dielectric loss ability at elevated temperatures and withstand the high-temperature oxidation, are optimum choices for HTMAMs^{15–17}. Some efforts have been made on fabricating ceramic-based HTMAMs, mainly focusing on non-oxide SiC-based^{13,14,18}, Si₃N₄-based^{5,17,19}, SiBCN-based^{10,20,21}, TiB₂-based^{11,22,23}, TiC-based²⁴, and Ti₃AC₂-based (A = Si or Al)^{25,26} materials. Nevertheless, these non-oxide HTMAMs have trouble in resisting long-term oxidative environment at elevated temperatures owing to the tendency of metal atoms to combine with oxygen in the high-temperature atmosphere in a long duration^{13,27}.

In comparison, oxide ceramics have much better long-time oxidative resistance at higher temperatures thanks to their oxidation states, which are thus considered as ideal candidates for HTMAMs in the extreme environment^{2,28}. However, most commonly seen single-phase simple oxides, such as MgO, Al₂O₃, TiO₂ (to name a few)^{11,23,29}, can hardly consume microwaves at different temperatures because of their poor dielectric loss ability arising from the deficiency of polarization or conduction mechanisms at GHz frequencies. To solve this issue, researchers have developed some strategies to introduce polarization mechanisms or electrical conduction within oxide ceramics. As for the polarization strategies, they have proposed metal doping for creating defect-induced polarization (Zn-doped Al₂O₃³⁰, La_{0.7}Sr_{0.3}Mn_{0.8}Fe_{0.2}O₃³¹), and high-entropy design for producing heterointerfacial polarization ((Fe_xCoNiCrMn)_yO_z^{6,32}). With regard to the generation of electrical conduction, they have also studied the incorporation of conductive oxides, such as La_{0.9}Sr_{0.1}MnO₃² and MgZr₄P₆O₂₄³³. Nevertheless, the dielectric polarization or electrical conduction of these reported oxide ceramic HTMAMs is still weak, which causes their limited permittivity and mediocre impedance matching, leading to their suboptimal high-temperature microwave-absorbing performance, *i.e.* narrow effective absorption bandwidth (EAB < 4 GHz) and unsatisfying minimum reflection loss ($R_{Lmin} > -40$ dB) at large thicknesses ($d \geq 1.5$ mm) at elevated temperatures. Accordingly, it is challenging to fabricate high-performance oxide ceramic HTMAMs that can accommodate severe environment for a long duration.

In this work, we employ rare earth zirconates, a kind of oxide ceramic with one-eighth vacancies in the anion sites which are stable up to 1600 °C in the atmosphere, as promising candidates for HTMAMs. The ultra-dense oxygen vacancies within these ceramics greatly reinforce the microwave-absorbing performance via thermionic migration at elevated temperatures, which results in a surge in permittivity to largely reduce material thicknesses. More importantly, the thermionic-facilitated permittivity can be meticulously tuned by electron delocalization among the adjacent lattice atoms, with the degree decided by the lattice disorder. The ordered pyrochlore-phase structure can trigger the contraction of electron delocalization, resulting in stronger thermionic migration and thereby slightly larger permittivity, and vice versa. This concept is demonstrated by proposing a dual-layer Er₂Zr₂O₇/Gd₂Zr₂O₇ architecture with ordered pyrochlore Gd₂Zr₂O₇ as lower lossy layer and disordered fluorite-phase Er₂Zr₂O₇ as upper matching layer for better impedance matching, which showcases a superior EAB up to 8.27 GHz and R_{Lmin} down to -64.61 dB at ultrathin thicknesses below 1.2 mm at 600 °C mainly through macroscopic interfacial resonance, far exceeding up-to-date HTMAMs. In addition, it also displays an ultralow thermal conductivity of 1.61 W·m⁻¹·K⁻¹ at 600 °C owing to the abundant oxygen vacancies, which can further cope with some special circumstances where thermal insulation is needed to protect metallic hot sections. Our work provides an innovative strategy for designing high-performance HTMAMs robust to the long-term oxygen-rich high-temperature environment via electron-delocalization-mediated thermionic migration in oxide ceramics, which propels the realization of structural-functional integrated materials in extreme environment applications.

Results

Compositional and microstructural characterizations of rare earth zirconates

In regard to the compositions and microstructures of Er₂Zr₂O₇ and Gd₂Zr₂O₇, comprehensive characterizations have been performed by utilizing different forms of samples. As shown in Fig. 1a, d, the shape and location of XRD patterns regarding Er₂Zr₂O₇ and Gd₂Zr₂O₇ are virtually identical in the single-layer and dual-layer samples, indicating that there is no difference in the composition and microstructure of these zirconates between the single-layer and dual-layer samples. More importantly, all the diffraction peaks in the measured XRD patterns of every sample are very consistent with their PDF cards (Supplementary Fig. S1) and the previous literature^{34–37} in terms of both position and relative intensity, signifying the successful fabrication of crystalline fluorite-phase Er₂Zr₂O₇ with a disordered structure, as well as pyrochlore-phase Gd₂Zr₂O₇ with an ordered structure, in all the samples, signifying the successful fabrication of crystalline fluorite-phase Er₂Zr₂O₇ with a disordered structure, as well as pyrochlore-phase Gd₂Zr₂O₇ with an ordered structure, in all the samples. Moreover, there is no unidentified diffraction peak in these measured XRD results, indicating the successful formation of crystalline Er₂Zr₂O₇ or Gd₂Zr₂O₇ phase without any impurity phase through the solid reaction method in all the samples.

The morphology of Er₂Zr₂O₇ and Gd₂Zr₂O₇ is shown in Fig. 1b, e, which clearly displays micron-sized crystal grains, substantiating their crystalline nature. Moreover, SEM images in Fig. 1b, e indicate the absence of noticeable pores, signifying the densification of sintered Er₂Zr₂O₇ and Gd₂Zr₂O₇ samples, which is corroborated by their ultrahigh relative density of >99%, as decided by the Archimedes method. In addition, SEM-EDS elemental mapping with a larger microscopic scale of tens of microns, and TEM-EDS elemental mapping with a smaller microscopic scale of a few microns, can confirm the absence of any impurity phase in the fabricated zirconate samples. As exhibited in Fig. 1g–l, the Er/Zr/O elements are uniformly distributed in the SEM image of Er₂Zr₂O₇, while the Gd/Zr/O elements also display homogeneous distributions in the SEM image of Gd₂Zr₂O₇. These phenomena also hold true in the TEM-EDS mapping of the rare earth zirconates (Supplementary Figs. S2, S3), substantiating the complete absence of any impurity phase in the zirconate samples as indicated by the XRD analysis.

Besides, to prove the disordered/ordered structure of the zirconates more directly, SAED analysis was conducted in the HRTEM characterizations with electron beams parallel to the [001] zone axis. Based on the indexing results in the XRD patterns (Fig. 1a, d) and the measurement of lattice spacing in the HRTEM images (Fig. 1c, f), it is discovered in the inserted images in Fig. 1c, f that compared with the case of Er₂Zr₂O₇, there is a new set of distinctly weaker diffraction spots in the case of Gd₂Zr₂O₇ (marked by yellow dashed circles), of which the indexed crystal planes cannot be found in the XRD pattern of Gd₂Zr₂O₇. This demonstrates the existence of superlattice pattern that represents the ordered structure with an altered translation group³⁸. In other words, the absence of superlattice pattern in the SAED image of Er₂Zr₂O₇ denote its disordered structure instead.

Temperature-dependent dielectric properties of rare earth zirconates

The disordered/ordered phase structures of the abovementioned rare earth zirconates largely influence their electrical behaviors and thus dielectric properties at distinct temperatures that are closely relevant to the abundant oxygen vacancies (Figs. 2 and 3). Figure 3a illustrates the presence of one-eighth intrinsic oxygen vacancies in the anion sites within the crystal unit cells of these zirconates (silver balls), revealing their ultrahigh concentration. These vacancies arise from the nonequivalent theoretical valence between erbium (or gadolinium) atoms and zirconium atoms in these zirconates, and are electrically neutral in

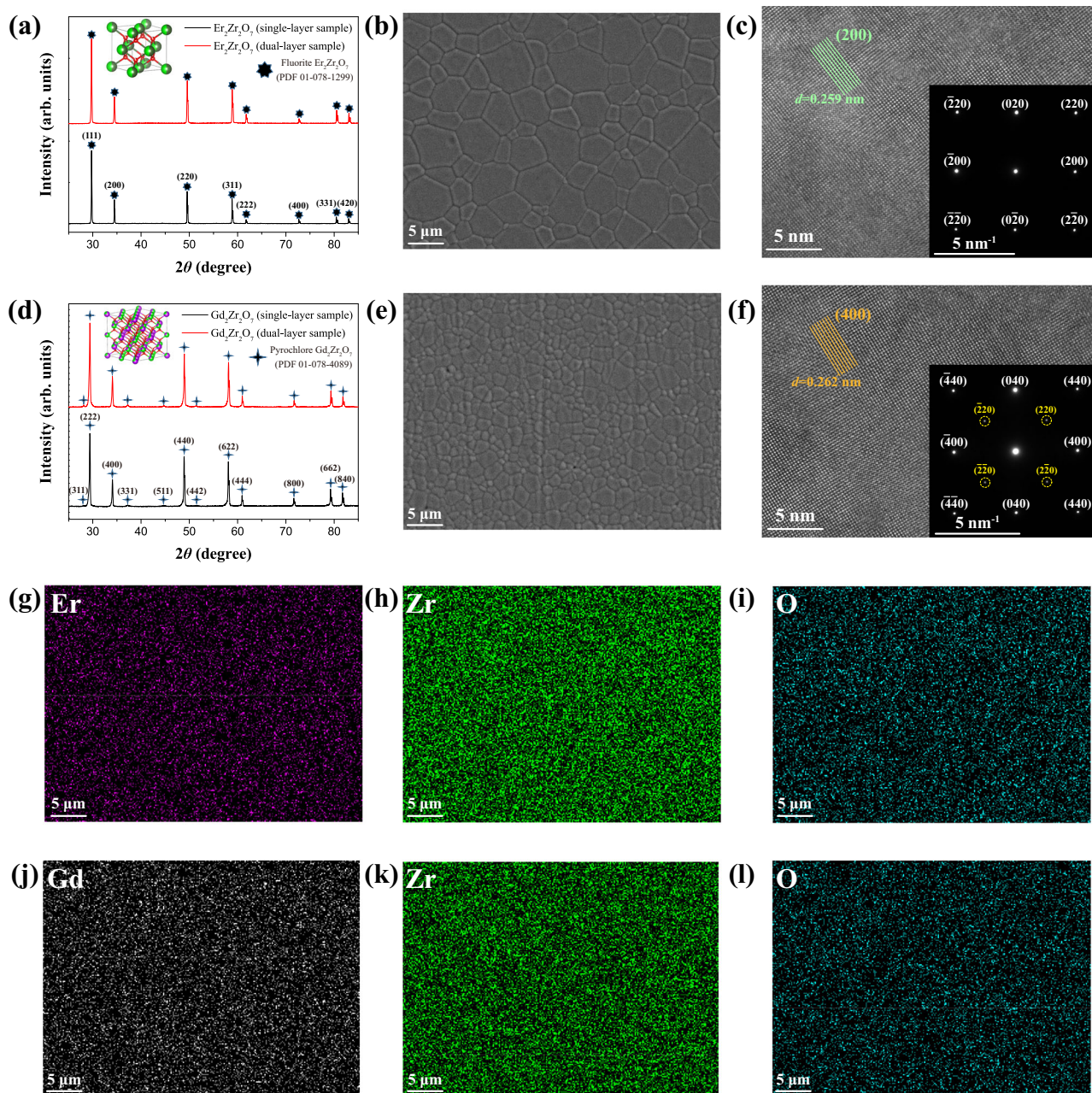


Fig. 1 | Compositions and microstructures of rare earth zirconates. **a** XRD patterns of $\text{Er}_2\text{Zr}_2\text{O}_7$ in the single-layer and double-layer structure. **b** SEM image of $\text{Er}_2\text{Zr}_2\text{O}_7$. **c** TEM image of $\text{Er}_2\text{Zr}_2\text{O}_7$ (with inserted SAED pattern). **d** XRD patterns of $\text{Gd}_2\text{Zr}_2\text{O}_7$ in the single-layer and double-layer structure. **e** SEM image of $\text{Gd}_2\text{Zr}_2\text{O}_7$.

f TEM image of $\text{Gd}_2\text{Zr}_2\text{O}_7$ (with inserted SAED pattern). **g–i** SEM-EDS elemental mapping images of $\text{Er}_2\text{Zr}_2\text{O}_7$. **j–l** SEM-EDS elemental mapping images of $\text{Gd}_2\text{Zr}_2\text{O}_7$. For SEM and TEM characterizations, three times were repeated independently with similar results in our study. Source data are provided as a Source Data file.

an ideal state. However, according to the O/Zr atomic ratios smaller than 3.5 as decided by EPMA measurement, $\text{Er}_2\text{Zr}_2\text{O}_7$ and $\text{Gd}_2\text{Zr}_2\text{O}_7$ samples also contain positively charged oxygen vacancies in practice in order to maintain overall electric neutrality (Supplementary Fig. S12).

As the temperature rises, ϵ' for these zirconates is observed to increase within the temperature range of RT - 400 °C (Fig. 2a, d, g). This enhancement is possibly due to the intensified ionic or electron displacement polarization with higher resonant frequencies far above GHz frequencies. In addition, it can also be discovered that the Lorentz dielectric resonant peaks in the ϵ'' - f curves shift to lower frequencies (Supplementary Figs. S5–S8), indicative of longer resonant times. This shift may be a result of the increased thermal vibration of oxygen

atoms at higher temperatures. An unusual observation is made for $\text{Gd}_2\text{Zr}_2\text{O}_7$, where the Lorentz dielectric resonance phenomenon present in the Ku band at temperatures ranging from RT to 400 °C disappears at 600 °C. Moreover, ϵ' of $\text{Gd}_2\text{Zr}_2\text{O}_7$ at 600 °C declines rapidly towards zero with increasing frequency and is significantly smaller than at 400 °C (Supplementary Fig. S8a, Fig. 2d). These phenomena can be ascribed to the dominance of conduction loss for $\text{Gd}_2\text{Zr}_2\text{O}_7$ due to its high ionic conductivity at 600 °C. The validity of this explanation is further supported by the nearly straight lines seen in the Cole-Cole plot of $\text{Gd}_2\text{Zr}_2\text{O}_7$ at 600 °C (Supplementary Fig. S10h), and more importantly, the basically larger dielectric loss ability at 600 °C compared to that at 400 °C for $\text{Gd}_2\text{Zr}_2\text{O}_7$ (Fig. 2e, f, h, i). Specifically, the upper and lower bounds of ϵ'' and α regarding $\text{Gd}_2\text{Zr}_2\text{O}_7$ at 600 °C are

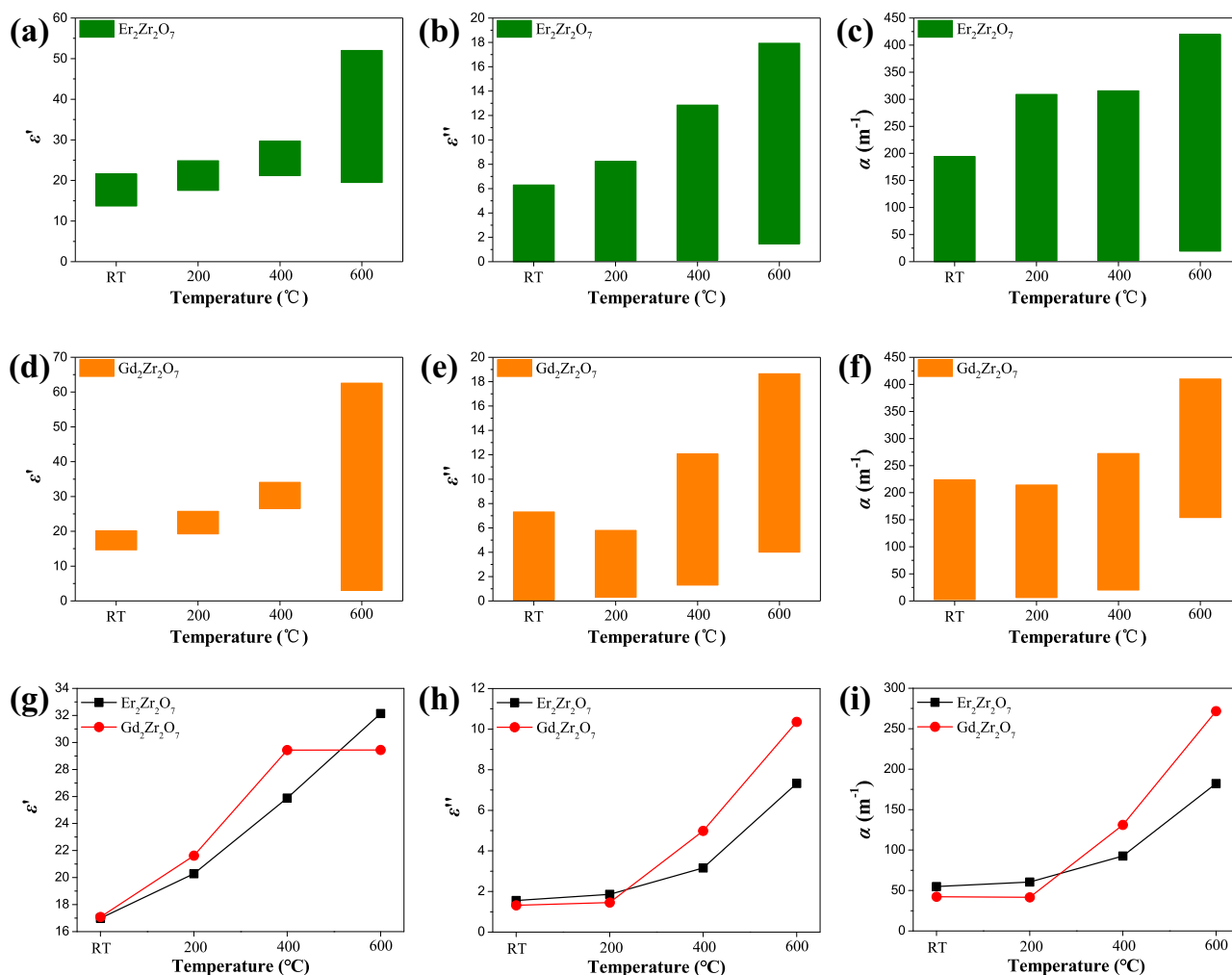


Fig. 2 | Dielectric properties at different temperatures of rare earth zirconates. Ranges of **a** ϵ' , **b** ϵ'' , and **c** α of $\text{Er}_2\text{Zr}_2\text{O}_7$ at different temperatures. Ranges of **d** ϵ' , **e** ϵ'' , and **f** α of $\text{Gd}_2\text{Zr}_2\text{O}_7$ at different temperatures. Comparison of average **g** ϵ' , **h** ϵ'' , and

i α of the discussed rare earth zirconates at different temperatures. Source data are provided as a Source Data file.

higher than that at other temperatures, and the trend of average α of $\text{Gd}_2\text{Zr}_2\text{O}_7$ surges with increasing temperature (Fig. 2i), which demonstrates the large rise in dielectric loss ability of $\text{Gd}_2\text{Zr}_2\text{O}_7$ at 600 °C.

Previous studies have shown that rare earth zirconates exhibit pure oxide-ion conduction at high temperatures (i.e. the long-range migration of oxygen atoms through the numerous paths set by oxygen vacancies in these lattices)^{39,40}, which can be generally described by the following Arrhenius formula³³:

$$\sigma = \sigma_0 \exp(-E_a/RT) \quad (1)$$

In Eq. (1), σ is the ionic conductivity, σ_0 is the preexponential factor signifying the ionic conductivity as the temperature approaches infinity, E_a is the apparent activation energy, R is the gas constant, and T is the temperature. According to the Arrhenius relationship, the natural logarithm of ionic conductivity should display a linear relationship with the reciprocal of the temperature. As demonstrated in Fig. 3d, the $(1/T, \ln\sigma)$ data points for both materials almost align in straight lines ($\ln\sigma = -14.74/T + 7.283$ for $\text{Er}_2\text{Zr}_2\text{O}_7$ and $\ln\sigma = -9.635/T + 3.209$ for $\text{Gd}_2\text{Zr}_2\text{O}_7$), indicating that the ionic conduction behaviors of these rare earth zirconates adhere to the Arrhenius relationship as the temperature rises. Furthermore, according to Fig. 3d, since the natural logarithm of ionic conductivity for these rare earth zirconates

is predicted to be so low (< -10) at temperatures not higher than 400 °C that the measurement errors may be severe, adopting linear extrapolation based on Fig. 3d is more reasonable to analyze the ionic conductivity of these zirconates below 600 °C. As shown in Supplementary Fig. S16, the ionic conductivity of these zirconates is considerably enhanced by many orders of magnitude with increasing temperature within the temperature range of RT - 600 °C.

Furthermore, it is noted in Fig. 3d and Supplementary Fig. S16 that the ionic conductivity of $\text{Gd}_2\text{Zr}_2\text{O}_7$ is generally higher than that of $\text{Er}_2\text{Zr}_2\text{O}_7$ within the temperature range of RT - 900 °C, despite the rapid growth of ionic conductivity with rising temperature for $\text{Er}_2\text{Zr}_2\text{O}_7$. This difference can be explained by the preexponential factors and apparent activation energy (Fig. 3e) in the Arrhenius relationship, based on the linear fitting of data points in Fig. 3d. The preexponential factor of $\text{Er}_2\text{Zr}_2\text{O}_7$ is notably larger than that of $\text{Gd}_2\text{Zr}_2\text{O}_7$, which may be ascribed to a higher total concentration of oxygen vacancies in the $\text{Er}_2\text{Zr}_2\text{O}_7$ sample. Nevertheless, the apparent activation energy of $\text{Er}_2\text{Zr}_2\text{O}_7$ is also substantially higher than that of $\text{Gd}_2\text{Zr}_2\text{O}_7$ because of the greater difficulty for oxygen atoms in $\text{Er}_2\text{Zr}_2\text{O}_7$ to move freely at elevated temperatures. As displayed in Fig. 3b, c, this difficulty emanates from the broader electron delocalization among the adjacent atoms, particularly between the nearest-neighbor rare earth atoms and oxygen atoms, and also

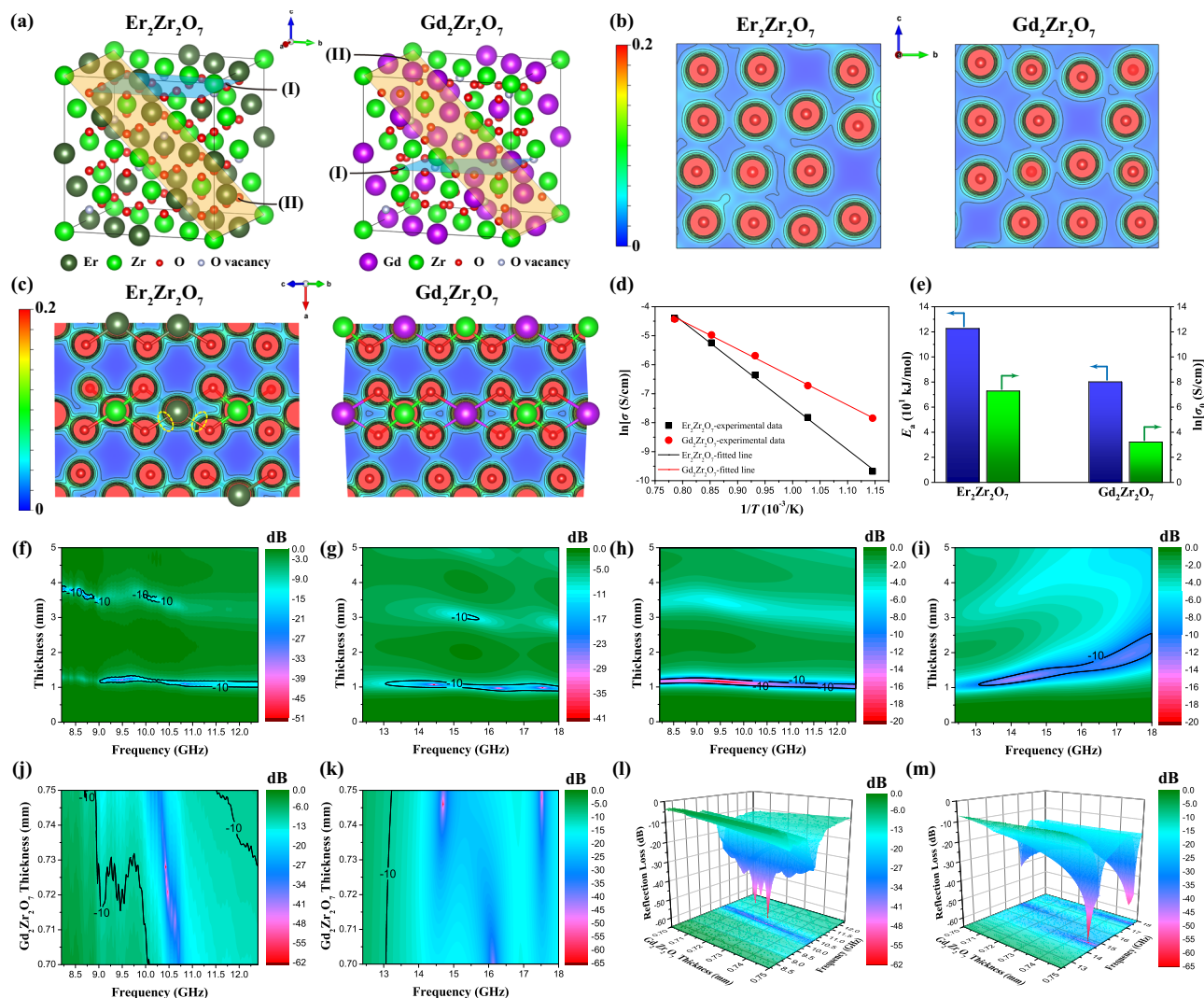


Fig. 3 | Dielectric loss mechanisms and microwave-absorbing performance of rare earth zirconates. a Selected crystal planes (I-II) in the lattices of these zirconates for charge density calculations. 2D charge density maps at **b** crystal planes (I) and **c** crystal planes (II). **d** Ionic conductivity with fitted lines. **e** Apparent activation energy and preexponential factor according to the Arrhenius equation. Microwave-

absorbing 2D plots of **(f, g)** $\text{Er}_2\text{Zr}_2\text{O}_7$ and **(h, i)** $\text{Gd}_2\text{Zr}_2\text{O}_7$ at 600 °C in the X-Ku bands. Microwave-absorbing **(j, k)** 2D and **(l, m)** 3D plots of dual-layer $\text{Er}_2\text{Zr}_2\text{O}_7/\text{Gd}_2\text{Zr}_2\text{O}_7$ structure at 600 °C in the X-Ku bands with a fixed thickness of 0.4 mm for $\text{Er}_2\text{Zr}_2\text{O}_7$ layer. Source data are provided as a Source Data file.

among the second-nearest-neighbor oxygen atoms, in the $\text{Er}_2\text{Zr}_2\text{O}_7$ lattice compared with the case of $\text{Gd}_2\text{Zr}_2\text{O}_7$. According to the previous literature^{41–43}, there is a prominent discrepancy in the apparent activation energy between the ordered pyrochlore-phase $\text{Gd}_2\text{Zr}_2\text{O}_7$ and the disordered fluorite-phase $\text{Gd}_2\text{Zr}_2\text{O}_7$, implying that the order-disorder phenomenon plays a pivotal role in the apparent activation energy of these zirconates via affecting the degree of electron delocalization in their lattices. As the oxygen vacancies are randomly distributed in each unit cell of fluorite-phase rare earth zirconates, the internal energy of these unit cells are different from each other, resulting in the tendency of establishing electron delocalization in these zirconates to equalize the internal energy and thereby stabilize their lattices. When the oxygen atoms in the lattices of fluorite-phase rare earth zirconates undergo the long-range migration, they have to overcome the higher energy barrier originating from the damage of broader electron delocalization state as compared with the case of ordered pyrochlore-phase rare earth zirconates, manifesting that the activation energy is larger for fluorite-phase rare earth zirconates than pyrochlore-phase ones. Since the ionic conduction at relatively lower temperatures is largely determined by the apparent activation

energy, the microstructure resistance of $\text{Gd}_2\text{Zr}_2\text{O}_7$ is speculated to be much lower than that of $\text{Er}_2\text{Zr}_2\text{O}_7$ within the temperature range of RT - 600 °C based on Supplementary Fig. S17, leading to higher ionic conductivity of $\text{Gd}_2\text{Zr}_2\text{O}_7$ compared to $\text{Er}_2\text{Zr}_2\text{O}_7$. Similar to electronic conductivity, ϵ'' is positively correlated with ionic conductivity as suggested by previous studies^{44,45}. This relation can elucidate the more pronounced dominance of ionic conduction in the dielectric loss of $\text{Gd}_2\text{Zr}_2\text{O}_7$ compared with that of $\text{Er}_2\text{Zr}_2\text{O}_7$, contributing to the noticeably larger extent of growth of ϵ'' and α for $\text{Gd}_2\text{Zr}_2\text{O}_7$ at 600 °C (Fig. 2b, c, h, i).

In addition, as for $\text{Er}_2\text{Zr}_2\text{O}_7$, it is observed from Supplementary Fig. S5 that the larger ϵ' decreases significantly with increasing frequency in the X band at 600 °C, contrasting with the stable and smaller ϵ' within the temperature range of RT - 400 °C. Furthermore, at 600 °C, ϵ' of $\text{Er}_2\text{Zr}_2\text{O}_7$ stabilizes (~20) at higher frequencies in the Ku band, while the lower bound of ϵ' regarding $\text{Er}_2\text{Zr}_2\text{O}_7$ at 600 °C is also smaller than that at 400 °C (Supplementary Fig. S6, Fig. 2a). These phenomena can be attributed to the predominance of thermionic relaxation polarization in $\text{Er}_2\text{Zr}_2\text{O}_7$ at 600 °C. Thermionic relaxation polarization, as opposed to ionic conduction, involves the short-range

migration of oxygen atoms through the abundant oxygen vacancies in the lattice, requiring a smaller activation energy thanks to the lower barrier height for oxygen atoms to move over a short distance^{46,47}. Specifically, the relaxation time of thermionic polarization is considerably reduced with increasing temperature as per the Arrhenius relationship akin to Eq. (1), resulting in a shift of thermionic relaxation polarization towards a higher frequency of ~11.5 GHz in the X band for Er₂Zr₂O₇ at 600 °C. The occurrence of thermionic relaxation polarization is not exclusive to Er₂Zr₂O₇; the presence of a semicircle corresponding to ~11.5 GHz in the Cole-Cole plot of Gd₂Zr₂O₇ at 600 °C (Supplementary Fig. S3g), which is analogous to the case of Er₂Zr₂O₇ at 600 °C (Supplementary Fig. S2g), indicates the emergence of thermionic relaxation polarization for Gd₂Zr₂O₇ at 600 °C as well. Moreover, the broader electron delocalization in the Er₂Zr₂O₇ lattice results in a higher activation energy for the short-range migration of oxygen atoms compared to Gd₂Zr₂O₇ at 600 °C, resulting in a less intense thermionic relaxation polarization in Er₂Zr₂O₇.

In summary, both permittivity and dielectric loss are improved for these zirconates as the temperature rises, significantly boosting their high-temperature microwave-absorbing performance (Supplementary Figs. S18, S19 and Fig. 3f–i). EAB for these zirconates increases dramatically with temperature, peaking at 600 °C (Supplementary Fig. S20 and Supplementary Table S1, S2). Furthermore, the heightened permittivity of these zirconates at elevated temperatures facilitates the reduction in thickness according to the Maxwell's equations, which shows a negative correlation between the matching thickness of MAMs and their permittivity⁴⁸.

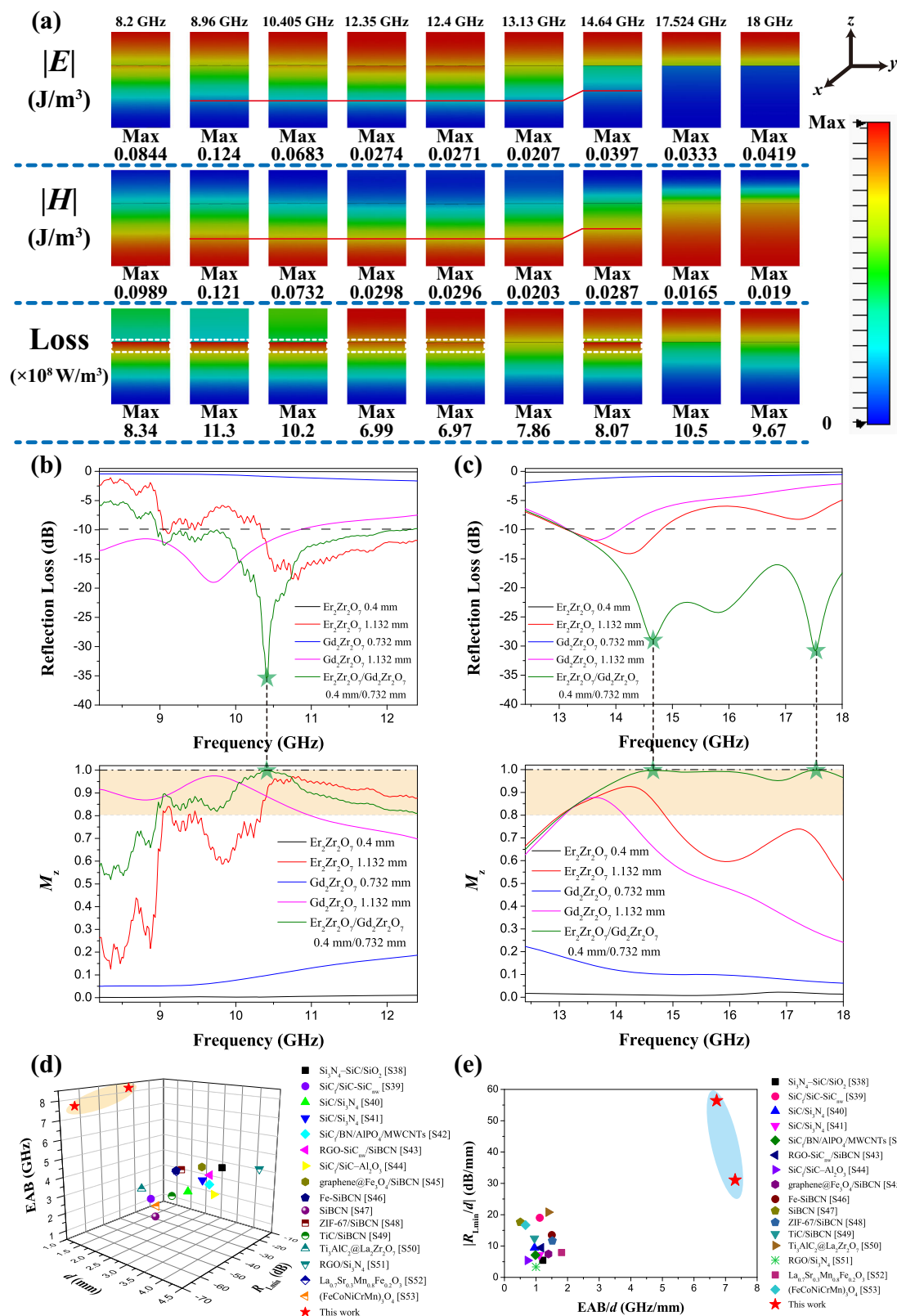
Enhanced microwave-absorbing performance of the dual-layer Er₂Zr₂O₇/Gd₂Zr₂O₇ architecture at 600 °C

Despite the improvement in EAB with increasing temperature for both Er₂Zr₂O₇ and Gd₂Zr₂O₇, R_{Lmin} for the single-layer of either zirconate display some degradation at 600 °C. More critically, the enhancement of EAB is constrained and does not span most of the X-Ku band. In addition, achieving a broader EAB and a lower R_{Lmin} at the same reduced thickness presents a challenge for single-layer rare earth zirconates at 600 °C. To address these issues, a dual-layer Er₂Zr₂O₇/Gd₂Zr₂O₇ architecture has been devised, which can realize “thin, wide and strong” simultaneously. As shown in Fig. 3h, i, the optimal thicknesses corresponding to the widest EAB of single-layer Er₂Zr₂O₇ and Gd₂Zr₂O₇ are located in the range of 1–1.2 mm. Hence, it is reasonable to deduce that the best EAB can be realized when the total thickness of the dual-layer structure is set in the range of 1–1.2 mm based on the general inverse correlation between permittivity (or frequency) and matching thickness with efficacious absorption. This viewpoint is substantiated by Supplementary Fig. S21 (or Supplementary Fig. S24), where almost all the combinations showcase an ultra-broadband EAB of at least 6 GHz with ultrathin total thicknesses in the range of 1–1.2 mm. Moreover, since the best R_{Lmin} and EAB in Supplementary Fig. S21 are better than that in Supplementary Fig. S24, the cases with fixed Er₂Zr₂O₇ layer are highlighted in this work. As shown in Supplementary Fig. S22, the R_{Lmin} of dual-layer structure with the fixed 0.4-mm-thick Er₂Zr₂O₇ layer is the lowest among all the circumstances of fixed thicknesses for the Er₂Zr₂O₇ layer at 600 °C. Moreover, Supplementary Fig. S23 reveals that the optimized case of 0.4-mm-thick Er₂Zr₂O₇ layer in the dual-layer structure at 600 °C showcases the widest EAB (8.27 GHz, when the thickness of Gd₂Zr₂O₇ layer is 0.732 mm) compared with other optimized cases of fixed thicknesses for the Er₂Zr₂O₇ layer. Consequently, a fixed thickness of 0.4 mm for Er₂Zr₂O₇ was reasonably set and investigated in depth, especially analyzing the best case (0.4 mm/0.732 mm, Fig. 3j–m).

As exhibited in Fig. 4a simulated from the CST Studio Suite 2018 software, in the dual-layer structure with the best thicknesses of 0.4 mm/0.732 mm at 600 °C, the intensity of power loss close to the Er₂Zr₂O₇/Gd₂Zr₂O₇ interface is noticeably higher than the adjacent

area at most of key monitoring frequencies below 17 GHz (marked by white dashed boxes, which represents the existence of macroscopic interfacial resonance), suggesting the importance of macroscopic interfacial resonance in boosting the impedance matching of the dual-layer structure to some extent. Based on Supplementary Fig. S23, the nature of macroscopic interfacial resonance is comprehensively investigated via analyzing the distribution of electric field, magnetic field, and power loss, regarding the dual-layer structure at 600 °C with these optimized thicknesses at several key frequencies. As exhibited in Supplementary Fig. S27, in respect to the circumstances in the X band particularly, the scope and degree of macroscopic interfacial resonance have a positive correlation with the microwave-absorbing performance of the dual-layer structure on the whole, further verifying the significance of macroscopic interfacial resonance, which is mainly triggered by the great difference of dielectric loss ability between Er₂Zr₂O₇ and Gd₂Zr₂O₇ in the X band. The broader electron delocalization in the Er₂Zr₂O₇ lattice causes weaker oxygen-related thermionic relaxation polarization and ionic conduction at 600 °C. Therefore, the dielectric loss ability of Er₂Zr₂O₇ at 600 °C is relatively weaker than that of Gd₂Zr₂O₇ at 600 °C. This makes Er₂Zr₂O₇ suitable for the upper matching layer in the dual-layer design to induce the incident microwaves to enter the lower lossy Gd₂Zr₂O₇ layer, which is crucial for generating the macroscopic interfacial resonance at the Er₂Zr₂O₇/Gd₂Zr₂O₇ interface for dissipating the microwaves at relatively lower frequencies effectively. In addition, the extent of macroscopic interfacial resonance is largely determined by the relative thickness of the Er₂Zr₂O₇ layer to the Gd₂Zr₂O₇ layer. It is revealed in Supplementary Fig. S27 that the smaller this relative thickness is, the larger intensity of electric field microwaves that go through the Er₂Zr₂O₇/Gd₂Zr₂O₇ interface are, thus resulting in the stronger dissipation of these microwaves to engender more prominent macroscopic interfacial resonance.

As for the connection between macroscopic interfacial resonance and impedance matching, the overall quarter-wavelength interference canceling effect is very crucial. As exhibited in Fig. 4a and Supplementary Fig. S27, in the cases about the dual-layer Er₂Zr₂O₇/Gd₂Zr₂O₇ structure that showcases efficacious microwave absorption in the X band, the distributions of electric or magnetic field are generally symmetric, while the phase difference between the electric and magnetic field is close to $\pi/2$, indicating the formation of standing waves within the dual-layer structure as a whole owing to the overall interference canceling effect⁴⁹. This can be further substantiated by the extensive intersections between the optimized range of total thicknesses regarding the dual-layer structure and the theoretical quarter-wavelength thickness curves of single-layer Er₂Zr₂O₇ or Gd₂Zr₂O₇ in the X band (Supplementary Fig. S28a), as well as the near-zero primary interfacial reflection energy coefficient at the Er₂Zr₂O₇/Gd₂Zr₂O₇ interface (R_{Eint}). The near-zero R_{Eint} in the X band stems from the similar values of ϵ' regarding these rare earth zirconates in the X band, to ensure the almost complete transmittance of microwaves through the Er₂Zr₂O₇/Gd₂Zr₂O₇ interface for setting up a solid foundation of achieving overall quarter-wavelength interference canceling in the X band. Thanks to the macroscopic interfacial resonance that reinforces the consumption of microwave energy in the X band effectively, the balance between the primary and high-ordered reflections at the air/Er₂Zr₂O₇ interface can be widely established, leading to the generation of overall quarter-wavelength interference, which contributes to the enhancement of impedance matching regarding the dual-layer structure in the X band. In addition, it is worth noting that especially for the cases in the Ku band, stronger degree of macroscopic interfacial resonance does not necessarily indicate more effective microwave-absorbing performance regarding the dual-layer structure. Owing much to the decreased wavelength of microwaves at higher frequencies, and the basically much higher attenuation constant of Er₂Zr₂O₇ in the Ku band compared with that in the X band, the



excessively intense macroscopic interfacial resonance will greatly suppress the high-order reflections at the air/ $Er_2Zr_2O_7$ interface, breaking the balance between the primary and high-order reflections at the air/ $Er_2Zr_2O_7$ interface, which is adverse to the realization of overall quarter-wavelength interference for strengthening impedance matching. Instead, relatively weaker macroscopic interfacial resonance is better when considering the cases in the Ku band.

On the other hand, with regard to the cases of the dual-layer structure above 17 GHz, no matter what degree of microwave absorption is, there is a total absence of macroscopic interfacial resonance in the distribution of power loss (Fig. 4a, Supplementary Fig. S27), indicating that the macroscopic interfacial resonance does not influence the microwave-absorbing performance above 17 GHz. Furthermore, the distributions of electric or magnetic field are

Fig. 4 | Analysis of microwave-absorbing properties of dual-layer Er₂Zr₂O₇/Gd₂Zr₂O₇ structure at 600 °C. **a** Spatial representation of the distribution of electric field ($|E|$, with units of J/m³; the red lines are the boundaries of blue areas), magnetic field ($|H|$, with units of J/m³; the red lines are the boundaries of red areas), and power loss (Loss, with units of $\times 10^8$ W/m³) at several key frequencies regarding the dual-layer structure (0.4 mm/0.732 mm, which are the thicknesses of Er₂Zr₂O₇/Gd₂Zr₂O₇ layer, respectively) based on CST calculations (the color scale bar has unit, and is relative to the spatial distribution of $|E|$, $|H|$, and Loss correspondingly; Max denotes the maximum value of $|E|$, $|H|$, or Loss at each corresponding spatial distribution, while white dashed boxes signify the presence of macroscopic

interfacial resonance). **b, c** Reflection loss curves and corresponding impedance coefficient curves for single-layer and dual-layer (0.4 mm/0.732 mm, which are the thicknesses of Er₂Zr₂O₇/Gd₂Zr₂O₇ layer, respectively) structures (the dotted -10 dB line in the reflection loss plots is a standard level of effective absorption, while the orange area in the impedance coefficient plots represents good impedance matching). **d, e** Comprehensive comparison of microwave-absorbing performance at 600 °C between state-of-the-art HTMAMs and the dual-layer structure (see Supplementary Table S3 for more details, refs. 38–53). Source data are provided as a Source Data file.

conspicuously asymmetric in the circumstances about the dual-layer structure that present effective microwave absorption above 17 GHz (Fig. 4a, Supplementary Fig. S27), which excludes the overall quarter-wavelength interference canceling effect as a potential reason to explain the phenomena of efficacious absorption above 17 GHz. It can be explained by Supplementary Fig. S28b, d, where the optimized range of total thicknesses regarding the dual-layer structure has no intersection with the theoretical quarter-wavelength thickness curves of single-layer Er₂Zr₂O₇ or Gd₂Zr₂O₇ above 17 GHz; meanwhile, particularly above 17 GHz, the primary interfacial reflection energy coefficient at Er₂Zr₂O₇/Gd₂Zr₂O₇ interface prominently deviates from 0, which greatly damages the foundation of the realization of overall quarter-wavelength interference canceling. In spite of this, another kind of interference canceling still exists in the cases that show effective microwave absorption above 17 GHz. The inverse distributions of electric and magnetic field within each layer in the dual-layer structure can be found in these cases basically, signifying the contribution of hierarchical interference canceling effect to the enhanced microwave-absorbing performance above 17 GHz. This is triggered by the abrupt decline of the intensity of electric field across the Er₂Zr₂O₇/Gd₂Zr₂O₇ interface, mainly deriving from the huge discrepancy of dielectric storage capability at 600 °C between Er₂Zr₂O₇ and Gd₂Zr₂O₇ above 17 GHz (Supplementary Figs. S6, S8). Specifically, due to the substantially lower ϵ' at 600 °C regarding Gd₂Zr₂O₇ (3–6) than that regarding Er₂Zr₂O₇ (~ 20) above 17 GHz, the dielectric storage capability of Gd₂Zr₂O₇ is much weaker than that of Er₂Zr₂O₇ at 600 °C, leading to the disparate distribution of electric and magnetic fields within each layer, which is conducive for the emergence of hierarchical interference canceling.

In view of these, the impedance coefficient (M_z), which characterize the degree of impedance matching with a positive correlation⁵⁰, is largely confined within the range of [0.8, 1] regarding the dual-layer Er₂Zr₂O₇/Gd₂Zr₂O₇ structures with the optimal thicknesses of 0.4 mm/0.732 mm, contributing to the remarkable expansion of effective absorption bandwidth for the dual-layer structure (Fig. 4b, c). Besides, the case with the thicknesses of 0.401 mm/0.745 mm, which has the lowest $R_{L\min}$ of -64.61 dB after some trials based on Supplementary Figs. S21, S24, is analogous to the case with the thicknesses of 0.4 mm/0.732 mm in terms of the microwave-absorbing mechanisms. Hence, the comprehensive microwave-absorbing performance of the dual-layer Er₂Zr₂O₇/Gd₂Zr₂O₇ structure at 600 °C is notably superior to that of the top-performing HTMAMs, with a maximum EAB/ d of 7.31 GHz/mm (0.4 mm/0.732 mm) and a maximum $|R_{L\min}|/d$ of 56.38 dB/mm (0.401 mm/0.745 mm), enabling the dual-layer structure as a competitive candidate for high-performance HTMAMs at 600 °C (Fig. 4d, e).

Thermal properties and microwave stealth ability of the dual-layer Er₂Zr₂O₇/Gd₂Zr₂O₇ structure

Apart from the superior microwave-absorbing performance, the dual-layer Er₂Zr₂O₇/Gd₂Zr₂O₇ structure also displays excellent thermal properties. As abovementioned, Er₂Zr₂O₇ and Gd₂Zr₂O₇ obtain ultra-dense oxygen vacancies, leading to the substantially improved ionic conduction at elevated temperatures. The rising ionic conduction

makes almost no contribution to the charge carrier term of thermal conductivity (κ_c , which is actually negligible owing to the absence of electron/hole conduction in these zirconates³⁹), and therefore does not affect the thermal conduction from the perspective of charge carrier transport^{51–53}. In the meantime, the abundant oxygen vacancies in these zirconates effectively shorten the phonon mean free path (λ) through the strong phonon scattering effect at oxygen vacancies^{35,54–56}, which thus largely curtail the lattice term of thermal conductivity regarding these zirconates ($\kappa_{\text{lat}} = C_v \lambda v / 3$, where C_v is the heat capacity, while v is the sound velocity)^{56,57}. Besides, with respect to the dual-layer Er₂Zr₂O₇/Gd₂Zr₂O₇ structure, the interfacial thermal resistance between the Er₂Zr₂O₇ and Gd₂Zr₂O₇ layer can further impede the thermal conduction through the whole structure. Consequently, despite the prominently larger thickness and relatively higher intrinsic κ of Gd₂Zr₂O₇ layer in the dual-layer structure, κ of the dual-layer structure at 600 °C is comparable to single-layer Er₂Zr₂O₇⁵⁸ instead of single-layer Gd₂Zr₂O₇⁵⁴ (Fig. 5a, b). Within the whole temperature range of RT–600 °C, κ of the dual-layer structure (1.58–1.94 W·m⁻¹·K⁻¹) are significantly smaller than that of yttria-stabilized zirconia (YSZ, 2.5–3 W·m⁻¹·K⁻¹)⁵⁸, the latter of which is commonly used as a type of thermal protection material, not to mention the existing HTMAMs. In other words, the dual-layer structure attains high conductivity and efficacious thermal insulation simultaneously at elevated temperatures thanks to the ultra-dense oxygen vacancies in the lattice of the rare earth zirconates inside the structure. In addition, both Er₂Zr₂O₇ and Gd₂Zr₂O₇ possess long-time thermal stability up to 1600 °C (See “S6. Interpretations of thermal tests” Section in the Supplementary Information for more details), signifying that the dual-layer Er₂Zr₂O₇/Gd₂Zr₂O₇ structure can endure extremely harsh environments considering the long-term shock-resistant properties of these zirconates previously reported by our group^{36,59–61}.

In addition, it is also important to assess the microwave stealth capabilities of the dual-layer Er₂Zr₂O₇/Gd₂Zr₂O₇ structure (0.4 mm/0.732 mm, which are the thicknesses of each layer respectively) at 600 °C in far-field conditions by calculating radar cross-section (RCS) in the CST Studio Suite 2018 software. As depicted in Fig. 5c–f, the monostatic and bistatic RCS curves for the dual-layer structure descends significantly compared with that for PEC side, the former of which is located below the -20 dBm² level (equivalent to the RCS level of small birds) across the entire incident angle range of $[-60^\circ, 60^\circ]$ ⁶². The substantial reduction of RCS regarding the dual-layer structure comprehensively signifies the imperceptible radar echo signals on the side of the upper Er₂Zr₂O₇ layer, which can be ascribed to the optimized impedance matching in the dual-layer architecture that preserves the strong absorption at higher incident angles (Supplementary Fig. S40). Particularly for the selected monitoring frequency of 10.405 GHz, the reflection loss is smaller than -10 dB at a high incident angle of 60° , contributing to the effective reduction of monostatic and bistatic RCS of the dual-layer structure compared with PEC even at higher incident angles. Moreover, in terms of the effect of RCS properties on the microwave-absorbing performance of the dual-layer structure, the substantially lower RCS at normal incidence of the dual-layer structure (0.4 mm/0.732 mm) than that of PEC in the whole X-Ku bands results in the efficacious and ultra-broadband RCS reduction at

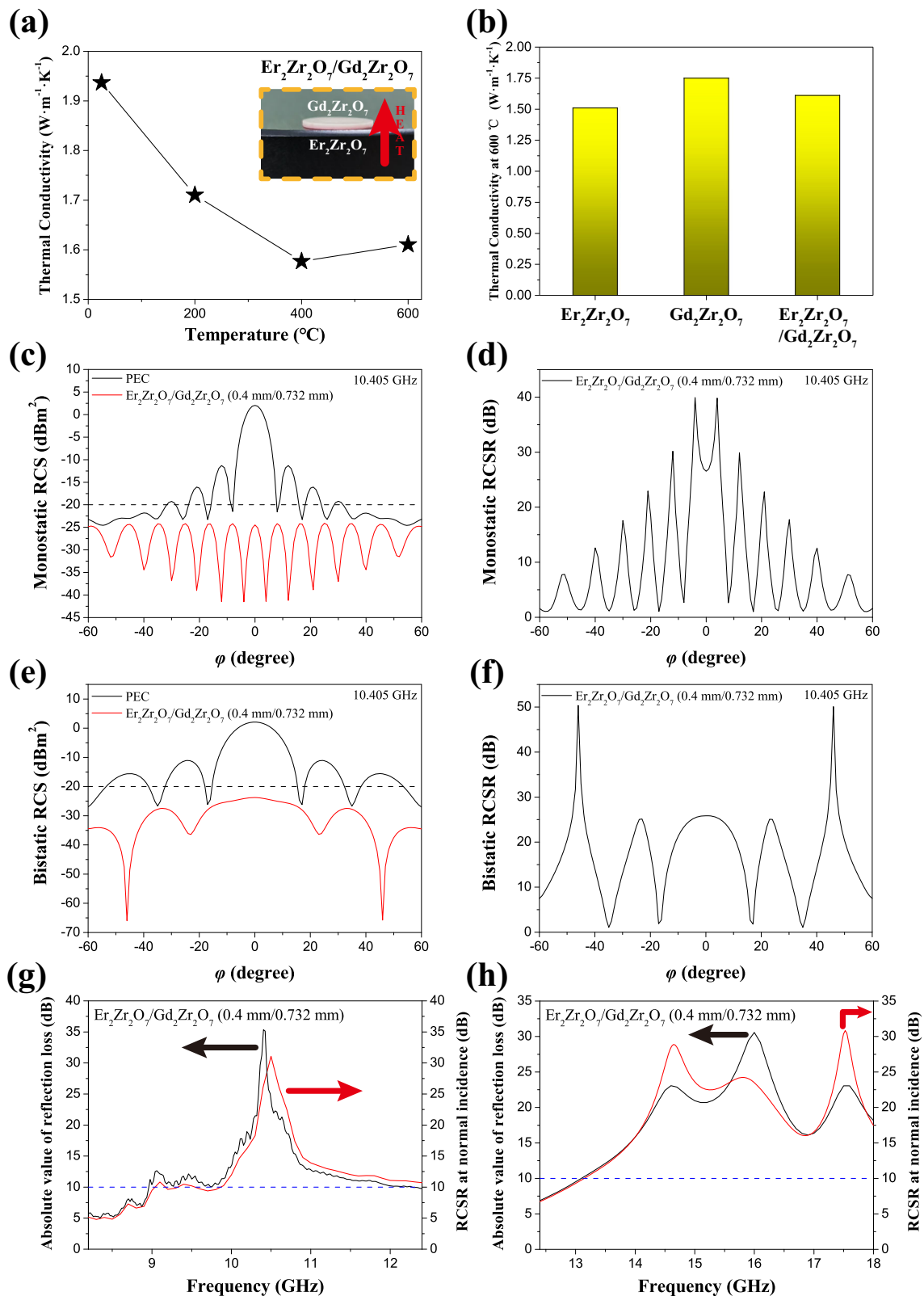


Fig. 5 | Thermal insulation and microwave stealth performance of dual-layer $\text{Er}_2\text{Zr}_2\text{O}_7/\text{Gd}_2\text{Zr}_2\text{O}_7$ structure. **a** Thermal conductivity of dual-layer $\text{Er}_2\text{Zr}_2\text{O}_7/\text{Gd}_2\text{Zr}_2\text{O}_7$ structure at different temperatures. **b** Comparison of thermal conductivity at 600°C between the dual-layer structure and each single-layer material. **c** Monostatic RCS curves regarding PEC and the dual-layer structure at 600°C (The dotted -20 dBm^2 line is the RCS level of small birds). **d** Monostatic RCSR curve of

the dual-layer structure at 600°C . **e** Bistatic RCS curves regarding PEC and the dual-layer structure at 600°C (The dotted -20 dBm^2 line is the RCS level of small birds). **f** Bistatic RCSR curve of the dual-layer structure at 600°C . **g, h** Comparison of reflection loss and RCSR at normal incidence in the X-Ku bands regarding the dual-layer structure at 600°C (The dotted 10 dB line is a standard level of effective absorption). Source data are provided as a Source Data file.

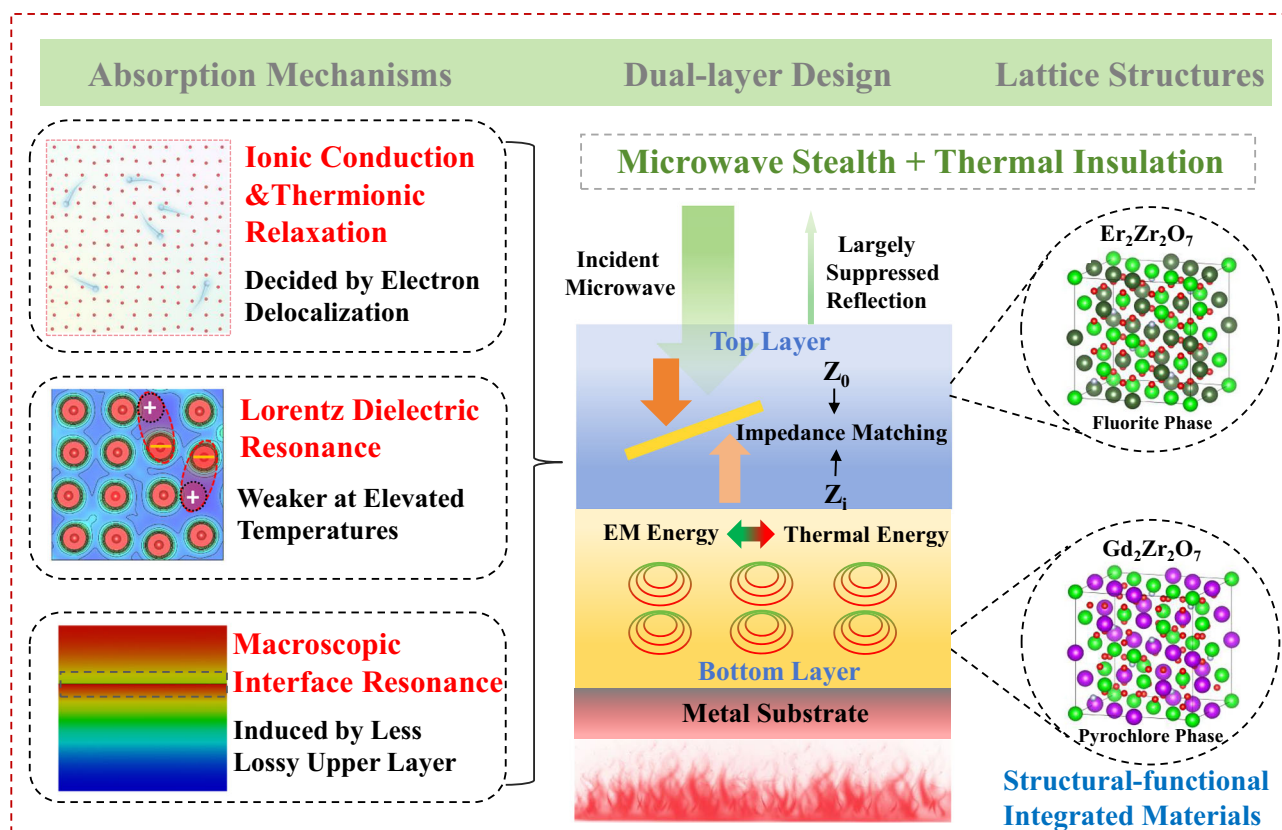


Fig. 6 | Schematic illustration of the various synergistic microscopic-macroscopic mechanisms of dual-layer $\text{Er}_2\text{Zr}_2\text{O}_7/\text{Gd}_2\text{Zr}_2\text{O}_7$ architecture. These mechanisms contribute to the exceptional high-temperature microwave-absorbing performance with thermal insulation.

normal incidence (7.73 GHz, with the criterion of $\text{RCSR} \geq 10 \text{ dB}^{63}$), which is similar to EAB of the dual-layer structure (Supplementary Fig. S41, Fig. 5g, h). This demonstrates that RCS reduction at normal incidence is closely and positively correlated with the microwave-absorbing performance. Therefore, the dual-layer $\text{Er}_2\text{Zr}_2\text{O}_7/\text{Gd}_2\text{Zr}_2\text{O}_7$ structure is competent to achieve outstanding microwave stealth in the electromagnetic monitoring environment at 600 °C.

Discussion

In summary, a dual-layer and oxygen-vacancy-enriched $\text{Er}_2\text{Zr}_2\text{O}_7/\text{Gd}_2\text{Zr}_2\text{O}_7$ architecture has been devised for high-performance and high-temperature microwave absorption in the X-Ku bands and long-term oxidative resistance up to 1600 °C (Fig. 6 and Supplementary Fig. S42). At elevated temperatures, oxygen atoms in the lattices of these zirconates can migrate through the stable oxygen vacancies with ultrahigh concentration in a short or long range, leading to the improving oxygen-related thermionic relaxation polarization and ionic conduction. This substantially improves the permittivity of these zirconates with increasing temperatures, beneficial for boosting their high-temperature microwave-absorbing performance with significantly reduced thicknesses. Furthermore, compared to the disordered fluorite-phase $\text{Er}_2\text{Zr}_2\text{O}_7$, the ordered pyrochlore-phase $\text{Gd}_2\text{Zr}_2\text{O}_7$ exhibits narrower electron delocalization, resulting in a lower activation energy of oxygen atoms and thus stronger thermionic migration. Consequently, $\text{Gd}_2\text{Zr}_2\text{O}_7$ basically obtains slightly larger permittivity than $\text{Er}_2\text{Zr}_2\text{O}_7$, contributing to the further optimization of impedance matching by proposing dual-layer architecture with the bottom-layer ordered $\text{Gd}_2\text{Zr}_2\text{O}_7$ and top-layer disordered $\text{Er}_2\text{Zr}_2\text{O}_7$ to induce macroscopic interfacial resonance for better impedance matching. As a result, the $\text{Er}_2\text{Zr}_2\text{O}_7/\text{Gd}_2\text{Zr}_2\text{O}_7$ structure demonstrates an ultrahigh EAB/ d up to 56.38 dB/mm and $|R_{\text{Lmin}}/d|$ up to 7.31 GHz/mm at ultrathin thicknesses below 1.2 mm at 600 °C. Besides, it also shows

an ultralow thermal conductivity of $1.61 \text{ W}\cdot\text{m}^{-1}\cdot\text{K}^{-1}$ at 600 °C, manifesting its exceptional thermal insulation. This work offers a promising route, namely thermionic migration mediated by electron delocalization, for fulfilling greatly enhanced microwave absorption in the long-time oxygen-rich high-temperature atmosphere, which may be extended to other types of oxide ceramics not limited to rare earth zirconates and other kinds of ion-conductive mechanisms not limited to oxygen conduction.

Methods

Raw materials

Metal oxide powders, including Er_2O_3 (purity $\geq 99.99\%$), Gd_2O_3 (purity $\geq 99.99\%$) and ZrO_2 (purity $\geq 99.99\%$) were purchased from Aladdin Industrial Corporation (Shanghai, China). Ethanol (purity $\geq 99.7\%$) was supplied by MREDA Technology Corporation (Beijing, China). All the chemical reagents were utilized without any purification.

Preparation of rare earth zirconates

$\text{Er}_2\text{Zr}_2\text{O}_7$ and $\text{Gd}_2\text{Zr}_2\text{O}_7$ rare earth zirconate powders were fabricated by the solid reaction method. Raw metal oxide powders (Er_2O_3 , Gd_2O_3 , and ZrO_2) were firstly pre-calcined at 1000 °C for 2 h in order to remove the adsorbed H_2O and CO_2 molecules. Then, these powders were mixed homogeneously according to the stoichiometric ratio of $\text{Er}_2\text{Zr}_2\text{O}_7$ and $\text{Gd}_2\text{Zr}_2\text{O}_7$ separately through ball milling at 250 r/min for 5 h, where ethanol and ZrO_2 balls were used as the mixing medium. The obtained slurries were subsequently dried by rotary evaporation and calcined at 1250 °C for 5 h to complete the solid reaction between raw powders. Afterwards, the calcined powders were ground and ball-milled at 250 r/min for 10 h with the same mixing medium. The powders after rotary evaporation were ground, sieved through a 200-mesh screen, and hydraulically pressed at 20 MPa for 5 min to generate green bodies. Eventually, these green bodies underwent cold isostatic

pressing at 220 MPa and pressureless sintering at 1600 °C for 10 h so as to obtain dense ceramic bulks.

Microstructure and compositional characterizations

The phase information about Er₂Zr₂O₇ and Gd₂Zr₂O₇ samples was identified by an X-ray diffractometer (XRD, Rigaku D/max 2500) with Cu K α radiation (40 kV, 150 mA) and with a scanning speed of 8°/min. The chemical environment of oxygen atoms in these rare earth zirconates was investigated by X-ray photoelectron spectroscopy (XPS, Thermo SCIENTIFIC ESCALAB 250Xi X-ray photoelectron spectrometer) using monochromatic Al K α ($h\nu = 1486.68$ eV) as the X-ray source. The cross-sectional morphology and EDS mapping of these zirconates was observed by a scanning electron microscope (SEM, Zeiss MERLIN VP Compact) at 15 kV. In order to underline the grain boundaries in the SEM characterization, fractured zirconate samples were thermal etched at 1550 °C for 30 min in advance. Before SEM observation, a high-vacuum sputter coater (Leica EM ACE600) was used to spray conductive platinum onto these fractured samples. The HRTEM images, TEM-EDS mapping, and SAED patterns of these zirconates after ion thinning were obtained by a transmission electron microscope (TEM, JEM-2100F, JEOL). The elemental composition of these rare earth zirconates was acquired by an electron probe microanalyzer (EPMA, JEOL JXA8230). The surface of these rare earth zirconates samples was polished before EPMA measurement.

Electrical measurement

For the purpose of reducing the error, the ionic conductivity of Er₂Zr₂O₇ and Gd₂Zr₂O₇ was measured at relatively higher temperatures (600–1000 °C, with an interval of 100 °C) by an AC impedance analyzer (CHI660E) sweeping from 100 Hz to 0.1 MHz. The complex permittivity of rare earth zirconate samples in the X-Ku bands at different temperatures (RT, 200 °C, 400 °C, and 600 °C) were tested by a vector network analyzer (VNA, Agilent-E5071C) with a heating device, where waveguide method was adopted with fixed complex permeability of 1-j0 (i.e. non-magnetic mode). Before VNA tests, waveguide samples with dimensions of 22.86 mm \times 10.16 mm \times 2 mm or 15.80 mm \times 7.90 mm \times 2 mm are cut from sintered ceramic bulks for the X or Ku band measurement respectively.

Thermal tests

The thermal diffusivity of the dual-layer Er₂Zr₂O₇/Gd₂Zr₂O₇ structure was tested by a laser flash instrument (Netzsch LFA 467), before which a disk-shaped dual-layer Er₂Zr₂O₇/Gd₂Zr₂O₇ sample was prepared with a diameter of 10 mm. Specifically, the sieved Er₂Zr₂O₇ and Gd₂Zr₂O₇ powders were weighed according to the ratio of thickness of each layer (i.e. 0.4:0.732 for the dual-layer Er₂Zr₂O₇/Gd₂Zr₂O₇ structure). After filling these powders into ϕ 15 mold successively, the layered powder was hydraulically pressed at 20 MPa for 5 min to generate green dual-layer body. Then, the green body experienced cold isostatic pressing at 220 MPa and pressureless sintering at 1600 °C for 10 h. Finally, the sintered dual-layer ceramic was machined to obtain a ϕ 10 sample, and the sample was sprayed with a thin graphite film before the thermal diffusivity test. Besides, the thermogravimetric measurement (TG, Mettler Toledo-TGA/DSC 3+) from room temperature (RT) to 1500 °C was performed in the air atmosphere.

Reporting summary

Further information on research design is available in the Nature Portfolio Reporting Summary linked to this article.

Data availability

All the data generated in this study are provided in the Supplementary Information/Source Data file. Source data are provided with this paper.

References

1. Li, G. et al. Temperature-induced self-decomposition doping of Fe₃GeTe₂ to achieve ultra-high T_c of 496 K for multispectral compatible strong electromagnetic wave absorption. *Adv. Funct. Mater.* **33**, 2210578 (2023).
2. Jia, H. et al. Enhanced high temperature microwave absorption of La_{0.9}Sr_{0.1}MnO₃/MgAl₂O₄ composite ceramics based on controllable electrical conductivity. *J. Eur. Ceram. Soc.* **40**, 1931–1937 (2020).
3. Cui, R. et al. Controlled deintercalation of graphene/organic superlattices with dense atomicscale steric Schottky heterojunctions for extreme microwave absorption. *Nat. Commun.* **16**, 5804 (2025).
4. Kim, S. H. et al. Carbon-based radar absorbing materials toward stealth technologies. *Adv. Sci.* **10**, 2303104 (2023).
5. Cai, Z. et al. Alternating multilayered Si₃N₄/SiC aerogels for broadband and high-temperature electromagnetic wave absorption up to 1000. *C. ACS Appl. Mater. Interfaces* **13**, 16704–16712 (2021).
6. Dai, G. et al. Evaluation and failure mechanism of high-temperature microwave absorption for heterogeneous phase enhanced high-entropy transition metal oxides. *Adv. Funct. Mater.* **34**, 2308710 (2023).
7. Liu, Y. et al. A highly deficient medium-entropy perovskite ceramic for electromagnetic interference shielding under harsh environment. *Adv. Mater.* **36**, 2400059 (2024).
8. Xia, Q. et al. High temperature microwave absorbing materials. *J. Mater. Chem. C* **11**, 4552–4569 (2023).
9. Wu, Z. et al. Dimensional design and core-shell engineering of nanomaterials for electromagnetic wave absorption. *Adv. Mater.* **34**, 2107538 (2022).
10. Luo, C. et al. Excellent electromagnetic wave absorption of iron-containing SiBCN ceramics at 1158 K high-temperature. *Adv. Eng. Mater.* **20**, 1701168 (2018).
11. Liu, X. et al. Enhancement on high-temperature microwave absorption properties of TiB₂-MgO composites with multi-interfacial effects. *Ceram. Int.* **47**, 4475–4485 (2021).
12. Qin, M. et al. Dielectric loss mechanism in electromagnetic wave absorbing materials. *Adv. Sci.* **9**, 2105553 (2022).
13. Han, T. et al. Effect of SiC nanowires on the high-temperature microwave absorption properties of SiCf/SiC composites. *J. Eur. Ceram. Soc.* **39**, 1743–1756 (2019).
14. Mu, Y. et al. Temperature-dependent dielectric and microwave absorption properties of SiC/SiC-Al₂O₃ composites modified by thermal cross-linking procedure. *J. Eur. Ceram. Soc.* **35**, 2991–3003 (2015).
15. Dai, G. et al. Quantitative evaluation of loss capability for in situ conductive phase enhanced microwave absorption of high-entropy transition metal oxides. *Adv. Funct. Mater.* **32**, 2205325 (2022).
16. Yang, J. et al. Microstructural evolution and electromagnetic wave absorbing performance of single-source-precursor-synthesized SiCuCN-based ceramic nanocomposites. *J. Adv. Ceram.* **12**, 1299–1316 (2023).
17. Li, M. et al. High-temperature dielectric and microwave absorption properties of Si₃N₄-SiC/SiO₂ composite ceramics. *J. Mater. Sci.* **50**, 1478–1487 (2014).
18. Wan, F. et al. Improved mechanical and high-temperature electromagnetic wave absorption properties of SiCf/BN/AlPO₄ composites with absorber multiwalled carbon nanotubes. *Composite Interfaces* **28**, 809–826 (2020).
19. Hou, Z. et al. Reduced graphene oxide/silicon nitride composite for cooperative electromagnetic absorption in wide temperature spectrum with excellent thermal stability. *ACS Appl. Mater. Interfaces* **11**, 5364–5372 (2019).

20. Chen, P. et al. Effect of boron content on the microstructure and electromagnetic properties of SiBCN ceramics. *Ceram. Int.* **48**, 3037–3050 (2022).
21. Luo, C. et al. Excellent electromagnetic wave absorption of MOF/SiBCN nanomaterials at high temperature. *Chin. J. Aeronautics* **34**, 277–291 (2021).
22. Liu, X. et al. Temperature-insensitive microwave absorption of TiB₂-Al₂O₃/MgAl₂O₄ ceramics based on controllable electrical conductivity. *Sci. China Technol. Sci.* **64**, 1250–1263 (2021).
23. Liu, X. et al. High-temperature dielectric and microwave absorption performances of TiB₂/Al₂O₃ ceramics prepared by spark plasma sintering. *Sci. China Technol. Sci.* **64**, 1264–1275 (2021).
24. Ding, J. et al. MXene-derived TiC/SiBCN ceramics with excellent electromagnetic absorption and high-temperature resistance. *J. Am. Ceram. Soc.* **104**, 1772–1784 (2020).
25. Su, J. et al. High-temperature dielectric and microwave absorption property of plasma sprayed Ti₃SiC₂/cordierite coatings. *J. Mater. Sci. Mater. Electron.* **27**, 2460–2466 (2015).
26. Sun, X. et al. Rational design of a core-shelled Ti₃AlC₂@La₂Zr₂O₇ composite for high-temperature broadband microwave absorption. *ACS Appl. Mater. Interfaces* **15**, 59895–59904 (2023).
27. Shi, R. et al. Influence of cobalt on the oxidation resistance of Al₂O₃-TiC composites at 800–1000°C in air. *Corros. Sci.* **88**, 101–108 (2014).
28. Jia, H. et al. Enhanced high temperature dielectric polarization of barium titanate/magnesium aluminum spinel composites and their potential in microwave absorption. *J. Eur. Ceram. Soc.* **40**, 728–734 (2020).
29. Fei, Y. et al. Recent progress in TiO₂-based microwave absorption materials. *Nanoscale* **15**, 12193–12211 (2023).
30. Wang, Y. et al. Enhanced dielectric properties and high-temperature microwave absorption performance of Zn-doped Al₂O₃ ceramic. *J. Electron. Mater.* **44**, 2353–2358 (2015).
31. Mu, Z. et al. The dielectric behavior and efficient microwave absorption of doped nanoscale LaMnO₃ at elevated temperature. *Nano Res.* **15**, 7731–7741 (2022).
32. Dai, G. et al. Entropy-driven phase regulation of high-entropy transition metal oxide and its enhanced high-temperature microwave absorption by in-situ dual phases. *J. Mater. Sci. Technol.* **116**, 11–21 (2022).
33. Li, M. et al. The conductivity, dielectric and electromagnetic attenuation properties of MgZr₄P₆O₂₄ ceramics at elevated temperature. *J. Eur. Ceram. Soc.* **40**, 5511–5517 (2020).
34. Vlášková, K. et al. Evidence for spin-glass ground state in fluorite-defect Er₂Zr₂O₇ single crystals. *Phys. Rev. B* **100**, 214405 (2019).
35. Wan, C. et al. Influence of B site substituent Ti on the structure and thermophysical properties of A₂B₂O₇-type pyrochlore Gd₂Zr₂O₇. *Acta Materialia* **57**, 4782–4789 (2009).
36. Qin, Y. X., et al. Low thermal conductivity ceramics for thermal barrier coatings. In: *4th China International Conference on High-Performance Ceramics (CICC-4)* (CICC, 2005).
37. Solomon, S. et al. Preparation, characterization, and ionic transport properties of nanoscale Ln₂Zr₂O₇ (Ln = Ce, Pr, Nd, Sm, Gd, Dy, Er, and Yb) energy materials. *J. Electron. Mater.* **44**, 28–37 (2014).
38. Williams, D. et al. *The Transmission Electron Microscope*, 2nd ed. (Springer, 2009).
39. Yamamura, H. et al. Electrical conductivity anomaly around fluorite-pyrochlore phase boundary. *Solid State Ion.* **158**, 359–365 (2003).
40. Zhang R., et al. Structure and ionic conductivity of Ln₂Zr₂O₇-type rare earth zirconates. In: *4th China International Conference on High-Performance Ceramics (CICC-4)* (CICC, 2005).
41. Vandijk, M. P. et al. Oxygen ion and mixed conductivity in compounds with the fluorite and pyrochlore structure. *Solid State Ion.* **9–10**, 913–919 (1983).
42. Diaz-Guillen, J. A. et al. Effect of La substitution for Gd in the ionic conductivity and oxygen dynamics of fluorite-type Gd₂Zr₂O₇. *J. Phys. Condens. Matter* **19**, 356212 (2007).
43. Rejith, R. S. et al. Influence of pyrochlore domains on the structure and electrical properties Gd_{2-x}Dy_xZr_{1.5}Hf_{0.5}O₇ energy materials. *J. Alloy. Compd.* **855**, 157291 (2021).
44. Meng, B. S. et al. Microwave absorption in insulating dielectric ionic crystals including the role of point defects. *Phys. Rev. B* **53**, 12777–12785 (1996).
45. Zhao, Z. et al. Hydro/organo/ionogels: “controllable” electromagnetic wave absorbers. *Adv. Mater.* **34**, 2205376 (2022).
46. Tan, R. et al. Ferrero Rocher® chocolates-like FeCo/C microspheres with adjustable electromagnetic properties for effective microwave absorption. *J. Alloy. Compd.* **857**, 157568 (2021).
47. Zhang, Z. et al. Constructing conductive network in hybrid perovskite for a highly efficient microwave absorption system. *Adv. Funct. Mater.* **32**, 2206053 (2022).
48. Cui, R. et al. Dielectric matching by the unique dynamic dipoles in hybrid organic/inorganic superlattices toward ultrathin microwave absorber. *Small* **19**, 2303008 (2023).
49. Tan, R. et al. PANI/FeCo@C composite microspheres with broadband microwave absorption performance. *Compos. Sci. Technol.* **218**, 109143 (2022).
50. Cai, B. et al. Interface-induced dual-pinning mechanism enhances low-frequency electromagnetic wave loss. *Nat. Commun.* **15**, 3299 (2024).
51. Wan, C. et al. Flexible n-type thermoelectric materials by organic intercalation of layered transition metal dichalcogenide TiS₂. *Nat. Mater.* **14**, 622–627 (2015).
52. Rice, M. J. et al. Ionic transport in super ionic conductors: a theoretical model. *J. Solid State Chem.* **4**, 294–310 (1972).
53. Bernges, T. et al. Considering the role of ion transport in diffuson-dominated thermal conductivity. *Adv. Energy Mater.* **12**, 2200717 (2022).
54. Yang, Z. et al. Near-infrared trapping by surface plasmons in randomized platinum-ceramic metamaterial for thermal barrier coatings. *Small Methods* **7**, 2201691 (2023).
55. Liu, X. et al. GdAlO₃/Gd₂Zr₂O₇ composites for advanced thermal barrier coatings. *J. Eur. Ceram. Soc.* **44**, 116736 (2024).
56. Wan, C. et al. Ultralow thermal conductivity in highly anion-defective aluminates. *Phys. Rev. Lett.* **101**, 085901 (2008).
57. Liang, J. et al. Polymer/carbon composites with versatile interfacial interactions for high performance carbon-based thermoelectrics: principles and applications. *Adv. Funct. Mater.* **33**, 2208813 (2022).
58. Yang, J. et al. Diffused lattice vibration and ultralow thermal conductivity in the binary Ln–Nb–O oxide system. *Adv. Mater.* **31**, 1808222 (2019).
59. Yang, Z. et al. Abnormal thermal expansion coefficients in (Nd_{1-x}Dy_x)₂Zr₂O₇ pyrochlores: the effect of low-lying optical phonons. *J. Adv. Ceram.* **12**, 1001–1014 (2023).
60. Zhu, B. et al. Enhanced sintering resistance in LaYbZr₂O₇ system through HfO₂ doping for thermal insulation ceramic materials. *J. Am. Ceram. Soc.* **107**, 7263–7273 (2024).
61. Han, Y. et al. Ultra-dense dislocations stabilized in high entropy oxide ceramics. *Nat. Commun.* **13**, 2871 (2022).
62. Zikidis, K. et al. Low observable principles, stealth aircraft and anti-stealth technologies. *J. Comput. Model.* **4**, 129–165 (2014).
63. Fang, G. et al. Determining the preferable polarization loss for magnetoelectric microwave absorbers by strategy of controllably regulating defects. *Chem. Eng. J.* **463**, 142440 (2023).

Acknowledgements

This work was primarily funded by National Natural Science Foundation of China within grant No. 52388201 and No. U23A6014 (to C.W.), No. 52271167 and No. 52473296 (to B.Z.), and No. 52305202 (to Z.D.).

Author contributions

R.C., Z.D., and C.W. initiated the concepts. R.C. and Z.D. designed the experiments. R.C., Z.D., G.Y., and L.Y. conducted the experiments. Y.L. performed the first principles calculations. R.C., Z.D., Y.L., X.L., B.Z., and C.W. analyzed the data. R.C., Z.D., Y.L., X.Z., X.L., B.Z., and C.W. wrote the manuscript. All the authors contributed to manuscript preparation.

Competing interests

The authors declare the following competing interests: C.W. (1st inventor, Tsinghua University), R.C. (2nd inventor, Tsinghua University), and Z.D. (3rd inventor, Tsinghua University) have applied for a Chinese patent that has been published and is under substantive examination (Application number CN118598661A). The patent covers the fabrication and application of dual-layer thermal insulating microwave absorbers with rare earth zirconates mentioned in this work. The other authors declare no competing interests.

Additional information

Supplementary information The online version contains supplementary material available at <https://doi.org/10.1038/s41467-025-64208-1>.

Correspondence and requests for materials should be addressed to Biao Zhao or Chunlei Wan.

Peer review information *Nature Communications* thanks Jia-Hu Ouyang, and the other, anonymous, reviewer(s) for their contribution to the peer review of this work. A peer review file is available.

Reprints and permissions information is available at <http://www.nature.com/reprints>

Publisher's note Springer Nature remains neutral with regard to jurisdictional claims in published maps and institutional affiliations.

Open Access This article is licensed under a Creative Commons Attribution-NonCommercial-NoDerivatives 4.0 International License, which permits any non-commercial use, sharing, distribution and reproduction in any medium or format, as long as you give appropriate credit to the original author(s) and the source, provide a link to the Creative Commons licence, and indicate if you modified the licensed material. You do not have permission under this licence to share adapted material derived from this article or parts of it. The images or other third party material in this article are included in the article's Creative Commons licence, unless indicated otherwise in a credit line to the material. If material is not included in the article's Creative Commons licence and your intended use is not permitted by statutory regulation or exceeds the permitted use, you will need to obtain permission directly from the copyright holder. To view a copy of this licence, visit <http://creativecommons.org/licenses/by-nc-nd/4.0/>.

© The Author(s) 2025